Journal of the Optical Society of America B
OPTICAL PHYSICS

Nonlinear optical fullerene and graphene-based polymeric 1D photonic crystals: perspectives for slow and fast optical bistability

Ivan M. Kislyakov,[1,2,3,8] Pavel V. Ivanov,[1,4] Jean-Michel Nunzi,[5] Andrey Yu. Vlasov,[4] Anton A. Ryzhov,[6] Anastasia V. Venediktova,[1,7] Hongqiang Wang,[1,2] Zixin Wang,[1,2] Tianju Zhang,[1,2] Ningning Dong,[1,2,3] and Jun Wang[1,2,3,*]

[1]Laboratory of Micro-Nano Optoelectronic Materials and Devices, Key Laboratory of Materials for High-Power Laser, Shanghai Institute of Optics and Fine Mechanics, Chinese Academy of Sciences (CAS), Shanghai 201800, China
[2]Center of Materials Science and Optoelectronics Engineering, University of Chinese Academy of Sciences, Beijing 100049, China
[3]CAS Center for Excellence in Ultra-intense Laser Science (CEULS), Shanghai 201800, China
[4]Institute of Chemistry, Saint Petersburg State University, St. Petersburg 198504, Russia
[5]Department of Physics, Engineering Physics and Astronomy and Department of Chemistry, Queen's University, Kingston, Ontario, K7L-3N6, Canada
[6]Institute of Radiation Physics, Helmholtz-Zentrum Dresden-Rossendorf, Dresden 01328, Germany
[7]Faculty of Physics, Saint Petersburg State University, St. Petersburg 198504, Russia
[8]e-mail: iv.kis@siom.ac.cn
*Corresponding author: jwang@siom.ac.cn

Received 19 April 2021; revised 13 July 2021; accepted 28 July 2021; posted 28 July 2021 (Doc. ID 428088); published 23 August 2021

Nonlinear optical (NLO) properties of materials can be enhanced by assembling them as thin polymer composite films alternating with other polymers and forming dielectric mirrors, 1D photonic crystals (1DPCs), wherein the input light intensity is increased. Based on the poly(vinyl carbazole) (PVK) and poly(vinyl alcohol) (PVA) contrasting polymer pair, variants of such structures, with graphene and fullerene in their high-index layers, have been produced. Their optical switching characteristics have been studied with ns, cw, and quasi-cw fs laser sources in the IR and with a fs laser in the visible range. We have demonstrated slow optical bistability in the polymeric 1DPCs determined by the thermal expansion of polymer composites at intensities over 100 W/cm^2 as well as fast and ultrafast optical switching due to thermo-optic and Kerr nonlinearities, respectively. Characteristic nonlinear refractive coefficients responsible for these processes were found to be $n_2^{to} \sim 10^{-1}$ cm^2/GW and $n_2^{Kerr} \sim 10^{-4}$ cm^2/GW. A subpicosecond fast spectral shift of the 1DPC bandgap has been found. Our results and analysis provide a clear picture of the NLO behavior of 1DPCs at different time scales. The results stimulate the subsequent design of ultrafast switches and bistable memory cells based on polymeric 1DPCs whose micrometer thickness and flexibility offer promise for implementation into fiber and microchip configurations.

https://doi.org/10.1364/JOSAB.428088

1. INTRODUCTION

The feature of the Fabry–Perot interferometer (FPI), filled with a nonlinear optical (NLO) substance, to switch at a certain intensity to a bistable state characterized with two different transmittance values is well known and has been intensively studied. Early experimental demonstrations of this effect, presented in the work of Gibbs *et al.* with sodium vapor [1], have triggered broad interest toward working out optical memory devices. This activity has been gradually getting more intense [2] in the light of the recent development in transmission and parallel processing of optical signals [3,4].

In a subsequent work, the Gibbs team demonstrated optical bistability in the FPI made of semiconductor material [5] and, finally, in a multilayer semiconductor mirror [6], consisting essentially of 61 identical FPIs stacked together. The latter system is a prototype of the objective of our research, the construction using periodically alternating layers of two materials with high (H) and low (L) refractive indices. In modern language, it is termed a one-dimensional (1D) photonic crystal (PC). Later, quite a lot of works were dedicated to the study of NLO properties [7,8] and optical bistability [9,10] of inorganic 1DPCs.

Subsequently, polymeric materials attract attention due to the achievement of a fairly good quality of the periodic structures

obtained on their base and unusual linear optical [11] and NLO [12] properties. Investigations of optical bistability in polymer-based 1DPCs, which is mostly determined by the typically small refractive index contrast, look scarce. The best performance of a thermo-optic bistability we know was obtained in a fiber-implemented design fabricated in the electron-beam resist ZEP520 with a high Q-factor [13]. In our work, we focus on another approach: to increase the contrast by choosing the optimal polymer pair, using a simple in-hand technology of spin-coating and neglecting to a certain extent the loss in the Q-factor. Such an approach gives us a favorable basis for the introduction of nanoparticles with high NLO properties.

Previously, we demonstrated [14] that the incorporation of graphene into a solution of poly(vinyl alcohol) (PVA) makes it possible to process a composite film by spin-coating, the film being compatible with another one of poly(vinyl carbazole) (PVK). The alternation of films forms 1DPC owing to a significant difference in the refraction of these polymers: $n_{\mathrm{PVA}} = 1.48$ (L); $n_{\mathrm{PVK}} = 1.68$ (H). We processed structures of the $g(\mathrm{HL})^N a$ type with the number of periods $N = 6$ and demonstrated a manifold-enhanced saturable absorption and the enhancement factor correlating with finesse F of the structures. Similar 12-fold enhancement of a NLO process of the opposite sign has been previously obtained in a metal-dielectric 1DPC bandpass filter [15].

It is worth noting that the enhancement of the electric field inside the 1DPC takes place mainly in the H-layer; in the case of our polymeric PCs, it was PVK. Thus, the purpose of the further development of the technology consisted in introducing graphene into PVK, increasing the depth (contrast) of the bandgap and its Q-factor at the cost of increasing the number and homogeneity of the layers. In the present work, an attempt was made to achieve these goals. We have fabricated several $g(\mathrm{LH})^N a$ structures with graphene dispersed in the H-layer with various concentrations at $N = 7$ and 10, and a structure with embedded C_{60} fullerene at $N = 10$. Studies of the third-order optical nonlinearity were performed in these structures with the search for optical bistability, the manifestation of which is expected in them. We present the results of these studies in this work.

The structure of this article is as follows. In Section 2, we describe the procedure of 1DPCs preparation alongside the nonlinear optical method used in the study of the samples. The results are discussed in Section 3. In Section 3.A, we show nanosecond Z-scan curves at the wavelength $\lambda = 1064$ nm and their fitting; therein, we connect the NLO absorption coefficients obtained with the NLO refraction coefficients related to a possible phase-shift under the assumption that it is the reason of the observed transmittance changes. In Section 3.B, we present the results obtained in continuous (cw) and quasi-continuous (qcw) regimes: bidirectional I-scans at $\lambda = 1064$ nm, the switching performance of 1DPCs coupled with the laser cavity, and tunable Z-scans of a 1DPC in the spectral range from 1020 to 1080 nm. We give semiquantitative evaluations of the observed phenomena in terms of thermo-optic phase shifts. In Section 3.C, we show femtosecond I-scan results at $\lambda = 520$ and 1040 nm of 1DPCs and transient absorption spectra in the visible range to reveal ultrafast NLO processes in the samples. The connection between the different pulse-length regimes is provided. Conclusions and perspectives are summarized in Section 4.

2. EXPERIMENTAL DETAILS

A. Photonic Crystals Preparation

All solutions for processing the photonic crystal were prepared by the weight method. The aqueous solution of PVA with a concentration of the polymer 2.7% wt. was kept at the temperature 60°C under continuous stirring for 2 h, while the PVK-toluene system (with polymer concentration 2.66% wt.) underwent mixing for 30 min.

Suspensions of graphene were prepared using the liquid phase exfoliation method [16]. First, graphite powder was ultrasonicated with a tip in the presence of the previously prepared PVK-toluene solution (60 min total duration in the 5″/5″ start/break regime), the initial concentrations of carbon equaling 15, 10, and 5 mg/ml for n0, n1, and n3 suspensions, respectively. An ice bath was used to cool the suspension during ultrasonication. Next, suspensions were centrifuged for 90 min at 1500 rpm and the supernatant was picked up. The triple system of C_{60}-benzene-PVK with a concentration of PVK 2.66% wt. was made by dissolving bulk polymer in a previously prepared 1 mg/ml solution of C_{60} in benzene. The presence of nanoparticles in the suspensions was determined by the absorption spectra (Fig. 1).

Based on a previously measured value of absorption cross-section of graphene in the suspension at $\lambda = 532$ nm: $\sigma_{\mathrm{Gr}} = 8000\ \mathrm{cm}^2/\mathrm{g}$ [17], graphene densities were found from the linear absorption coefficient: $\rho_{\mathrm{Gr}} = \alpha/\sigma_{\mathrm{Gr}} = 11.0\ \mu\mathrm{g/ml}$ (n0); 5.8 μg/ml (n1); 4.0 μg/ml (n3).

Periodic structures of 1DPCs consisting of alternating layers of PVA and either graphene-based PVK or C_{60}@PVK nanocomposite were obtained using the spin-coating method on a glass substrate. The PVA aqueous solution was spin-coating the substrate for 30 s at 1500 rpm and for 90 s at 600 rpm. Carbon nanomaterials mixed in PVK-toluene and PVK-benzene matrix (Gr@PVK, C_{60}@PVK, respectively) were spread with spin-coating for 30 s at 1500 rpm and for 90 s at 4000 rpm. The samples prepared were labeled as follows: PC1: Gr@PVK/PVA 14 layers, PC2: C_{60}@PVK/PVA 20 layers, and PC3: Gr@PVK/PVA 20 layers.

Nanoparticle densities inside the polymer ρ^p can be found from their densities in the suspension by multiplying the latter

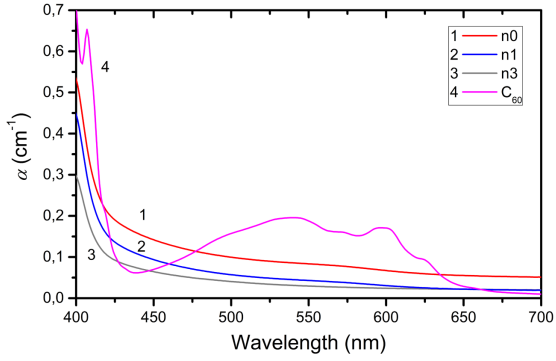

Fig. 1. Absorption spectra of Gr-PVK toluene and C_{60} benzene suspensions used for 1DPCs preparation.

by the PVK density ratio in the solid state and in the solution $f_d = 1.2/0.0231 = 52$.

B. Nonlinear Optical Study

The NLO study of thin polymer films is associated with difficulties that arise from the generally strong heterogeneity of the thickness, which is particularly dramatic when the thickness is of the order of the wavelength. Traditional effective methods for studying third-order nonlinearity produce significant distortions: Z-scan shows surface-quality-dependent profiles, often asymmetric irrespectively of the input energy, whereas an I-scan loses its sensitivity in the case of probing a vanishingly small layer on the background of the bulk materials (such as the substrate and attenuating filters). Taking this into account, we used collected statistics of scans and selected a method that better revealed the phenomena under the given conditions.

Nanosecond nonlinear optical response of 1DPCs was studied by the open-aperture Z-scan with the use of the Continuum Minilite II laser operating at $\lambda = 1064$ nm, focused by a 10 mm lens, repetition rate equaling 10 Hz with pulse duration $\tau_p = 7$ ns. Beam waist radius measured by an Ophir Spiricon beam profiler was $w_0 = 90 \pm 10$ μm. Input pulse energy was detected by a coherent energy meter and spanned the range 1–100 μJ. Larger energies were found able of damaging the polymeric films.

The cw MSI-III-1064-500mW laser and the coherent Chameleon 80 MHz repetition rate 140 femtosecond pulsed laser were used to explore the NLO behavior of 1DPCs in cw and qcw regimes, respectively. The latter was provided by the fast repetition of the fs laser yielding the train of pulses with 12.5 ns period, which is much faster than thermal relaxation in thin polymer films (the characteristic cooling time $t_c \sim l^2/a_t = 10$ μs for $l = 1$ μm of PVA with thermal diffusivity $a_t = 900$ cm^2/s [18]. Constant signals were registered with amplitude modulation provided by a chopper at a frequency of 50–200 Hz in the case of the cw laser and 400 Hz in the case of the qcw laser. Acquisition time was set >30 s to avoid transient processes. The input average power was controlled by a Thorlabs S470C thermal power sensor. The beam waists after focusing amounted to 60.4 ± 0.5 μm for cw and from 17 to 27 μm for qcw beams.

A Spectra Physics Spirit laser system was exploited for the I-scan and transient spectroscopy, operating at $\lambda = 1060$ nm, $\tau_p = 350$ fs, and $f_{rep} = 1$ kHz. A BBO crystal was used to generate the visible beam at $\lambda = 520$ nm. The beam was focused onto the sample with a 5 × /0.12 Leica objective and projected by a 50 × /0.55 objective to a DigiRetina 16 camera to control the sample position at the focal point and to measure the beam waist $w_0 = 13.3$ (520 nm) and $w_0 = 17.7$ (1040 nm). The ultrafast dynamics was studied by the transient spectroscopy using the same laser at $\lambda = 520$ nm as pump. The beam was split in two parts, one of which generated a supercontinuum in the wavelength window of 450–750 nm, the latter being used as a probe source. A motorized delay line scanned the time delay between the pump and probe up to 1.5 ns with a resolution of 12.5 fs. The pump and probe beams were focused on the sample at a magic angle, and the pump intensities achieved 23 GW/cm^2. The spectra were registered by a spectrometer and processed by a personal computer.

In all of the Z-scan and I-scan experiments, Thorlabs silicon detectors equipped with blinds to avoid light striking were used for simultaneous measurements of input and output signals.

3. RESULTS AND DISCUSSION

A. Linear Spectra and Inner Light Intensity Distributions

The obtained PC1, PC2, and PC3 are shown in Fig. 2. The samples are characterized by noticeable inhomogeneity, especially in the peripheral areas, whereas the central zones are sufficiently uniform. The linear transmission spectra of the PCs measured in their centers using a Perkin Elmer Lambda 750 UV/VIS/NIR spectrometer are also presented in Fig. 2. Each sample is characterized by two bandgaps (reflection maxima), the first one in the IR, the other in the visible region. The second bandgap in PC2 is smoothed by the large fullerene absorption in the visible range, but the IR bandgaps are well pronounced. We see that a larger number of layers provides deeper and narrower wells. Numerical characteristics of the bandgaps, i.e., positions of minima λ_{min}, Q-factors: $Q = \lambda_{min}/\Delta\lambda_{FWHM}$; contrast: $\gamma = (1 - T_{min})/(1 - T_{max})$; finesse: $F = 2\pi\sqrt{(\gamma - 1)}$ are given in Table 1.

Based on the matrix method [19], transmission spectra and light intensity redistributions inside the 1DPCs were simulated with fitting the layer thicknesses as parameters. For these calculations, refractive index dispersions were taken in accord with Sellmeier-type formulae: $n = 1.46 + 0.00665/\lambda^2$ for PVA [20] and $n = 2.3583 + 115869/(\lambda^2 - 33521.5)$ for PVK [21].

The evaluated concentration of graphene does not have any noticeable impact on the refractive index, whereas the effect of

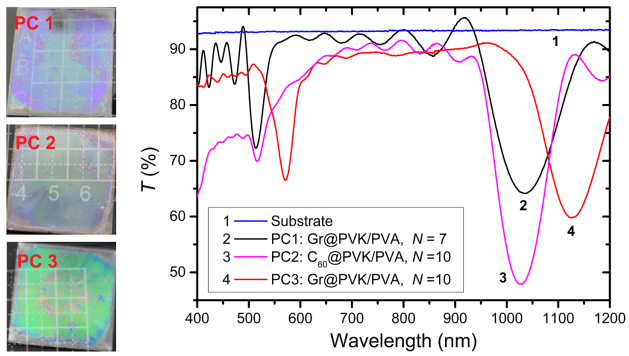

Fig. 2. 1DPCs and their transmission spectra.

Table 1. Linear Characteristics of 1DPCs

Sample	λ_{min} (nm) IR/Vis	Q (IR)	γ	F	l_1 (nm)	l_2 (nm)	f_{fe}
PC1, $N = 7$	1034/528	8.0	4.6	12	179	160	1.16
PC2, $N = 10$	1029/529	9.9	5.4	13	171	165	1.50
PC3, $N = 10$	1126/578	9.3	4.0	11	225	140	0.83

C_{60} needs to be considered. The complex refractive index of C_{60}@PVK composite was evaluated by the Sellmeier formula given in [22] and was added to the refractive index of PVK in accordance with the Maxwell Garnett equation [23]:

$$n = n_{\mathrm{PVK}}\sqrt{\frac{1+2f_{C_{60}}\Delta_r\varepsilon}{1-f_{C_{60}}\Delta_r\varepsilon}}, \quad \Delta_r\varepsilon = \frac{\varepsilon_{C_{60}}-\varepsilon_{\mathrm{PVK}}}{\varepsilon_{C_{60}}+2\varepsilon_{\mathrm{PVK}}}, \tag{1}$$

where $\varepsilon_{C_{60}}$ and $\varepsilon_{\mathrm{PVK}}$ are permittivity of fullerene and PVK, respectively, and $f_{C_{60}}$ is the fullerene density fraction.

The simulated spectra and intensity distribution inside 1DPCs for PC1, PC2, and PC3 are shown in Fig. 3. The simulations produce an average systematic shift of 11 nm in the second bandgap in the green region, whose position and amplitude are sensitive to the PVK dispersion. The latter is known for a large spread; further, additional available experimental data [24] look grossly underestimated even when compared with the value $n(589\ \mathrm{nm}) = 1.683$ provided by Sigma Aldrich, whose product we used. The application of this dispersion in our simulations led to the larger shape discrepancies of both bandgaps, meanwhile improving the position of the second one. Despite the said error, our simulations give an unambiguous result on the thickness of the layers, which are in accordance with a control made by atomic force microscopy, i.e., scanning the film incision showed the thicknesses of the layers in PC1 within 150–180 nm, however, without an attribution to the polymer type.

The simulation also gives the distribution of the field intensity inside the structures; it is shown for $\lambda = 1064$ nm in Figs. 3(b), 3(d), and 3(f). We can see that the light field has maxima inside PVK layers in PC1 and PC2, whereas, in the case of PC3, whose bandgap is not in a good resonance with this wavelength, the maxima are displaced to PVA layers. The field enhancement factors, $f_{\mathrm{fe}} = \int_0^{l_1} I(l)\mathrm{d}l/l_1 I_0$ (maximal enhancement achieved in the first PVK layer), along with the thicknesses of PVK (l_1) and PVA (l_2) layers are also given in Table 1.

B. Nanosecond Response

The normalized transmittance $T_{\mathrm{norm}} = T/T_{\mathrm{lin}}$ obtained by the Z-scan for PC1 and PC2 is shown in Fig. 4. The asymmetry of the curve stems from the inhomogeneity of the films, which manifests itself with small transverse displacements of the sample during the scanning. All films demonstrate a combination

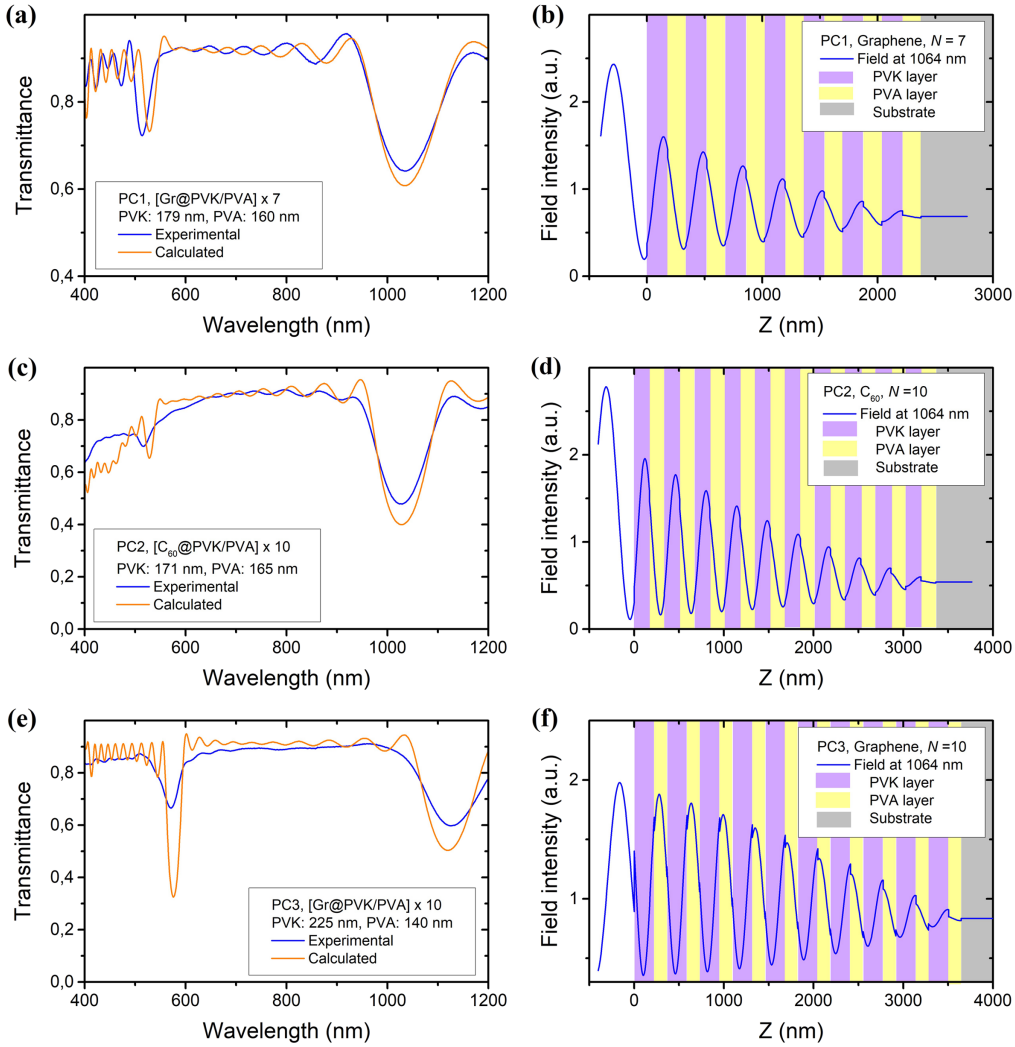

Fig. 3. Simulated spectra and light field intensity distributions at $\lambda = 1064$ nm for (a), (b) PC1, (c), (d) PC2, and (e), (f) PC3, respectively.

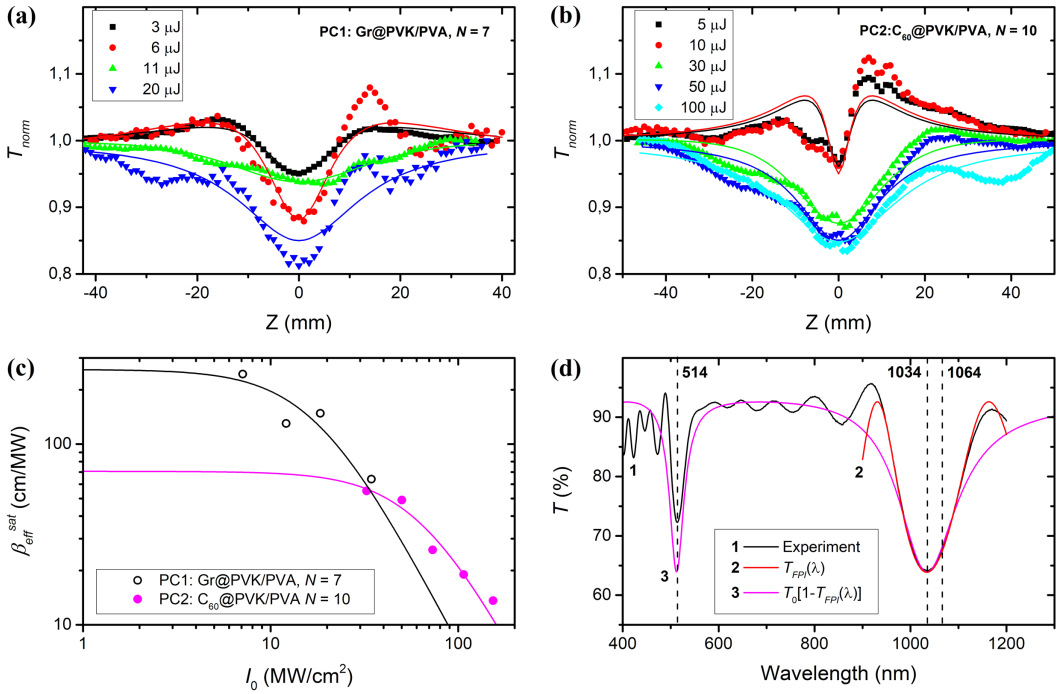

Fig. 4. Open-aperture Z-scan at 1064 nm of (a) PC1 and (b) PC2 at different input energies E_p (shown in the legends). (c) Input intensity dependence of the effective nonlinear absorption coefficients for PC1 and PC2. (d) Fitting of the spectrum of PC1 by the Fabry–Perot transmission functions.

of bleaching and limiting with the prevailing of the former, especially at higher input energies. No palpable NLO behavior over the ~ 4% background of film roughness was found in PC3.

The general consideration of nonlinear transmission, including manifestations of saturable absorption (SA) and two-photon absorption (TPA), can be made by solving the equation

$$\frac{dI(z)}{dz} = -\alpha I(z)\left(1+\left(\frac{I(z)}{I_{\mathrm{sat},\alpha}}\right)^{n_\alpha}\right)^{-1} - \beta_{\mathrm{eff}} I(z)^2\left(1+\left(\frac{I(z)}{I_{\mathrm{sat},\beta}}\right)^{n_\beta}\right)^{-1}, \quad (2)$$

where a Gaussian-beam intensity profile is assumed:

$$I(z) = \frac{E_p \pi w_0^2}{\tau_p\left(\pi^2 w_0^4 + z^2\lambda^2\right)}. \quad (3)$$

We fit our results with the ordinary model of SA in semiconductors with hyperbolic dispersions, assuming $n_\alpha = 1$, and nonsaturable TPA, i.e., $I_{\mathrm{sat},\beta} = \infty$. The quantities $I_{\alpha s}$, w_0, α_0, and β_{eff} were the fitting parameters. The second term in Eq. (2) in our case may be caused by a shift of the PC bandgap: In the linear regime, $T(1064\,\mathrm{nm}) > T_{\min}(1030\,\mathrm{nm})$ for both PC1 and PC2, and a redshift of the spectrum should result in a decrease of transmittance. The obtained effective NLO absorption coefficient turns out to be saturated, $\beta_{\mathrm{eff}}^{\mathrm{sat}}$, both for PC1 and PC2. Its dependences on the input intensity $I_0 = E_p/(\tau_p \pi w_0^2)$ shown in Fig. 4(c) were subsequently fitted by the homogeneously broadened β-saturation model: $\beta_{\mathrm{eff}}^{\mathrm{sat}} = \beta_{\mathrm{eff}}/[1+(I/I_{\mathrm{sat},\beta})^2]$ by varying β_{eff} and $I_{\mathrm{sat},\beta}$ [25]. These two steps of fitting were necessary to decrease the number of simultaneous parameters in Eq. (2) and thereby increase the sensitivity of the data analysis. The resulting fitting parameters are given in Table 2. Being determined by a bandgap shift, β_{eff} is limited by the minimal transmittance value and hence must be saturated. Therefore, our observations confirm the bandgap shift assumption.

Table 2. Phase Factor and NLO Parameters: Second-Order Saturation Intensity, Effective Nonlinear Absorption Coefficient, and the Resulting Nonlinear Refractive Index of PC1 and PC2 at λ = 1064 nm

Sample	f	$I_{\mathrm{sat},\beta}$ (MW/cm²)	β_{eff} (cm/MW)	n_2 (cm²/GW)
PC1: Gr@PVK/PVA, $N=7$	0.232	17.7	259	0.360
PC2: C_{60}@PVK/PVA, $N=10$	0.577	64.8	70.7	0.244

A 1D-PC can be considered as a set of identical Fabry–Perot interferometers (polymer layers). In this regard, it is logical to assume that the spectral shape of the bandgap center can be well described by the transmission function of the interferometer [26]. For the zero-order interference minimum, one has

$$T_{\mathrm{FPI}}(\lambda) = \frac{T_{\mathrm{out}}}{1 + F\sin^2\left[\delta_0(\lambda)\right]}. \quad (4)$$

Here, T_{out} is the transmittance outside the bandgap. The phase is $\delta_0(\lambda) = 2\pi n_0 L/\lambda$, where n_0 is the linear refractive index and L is the layer thickness. The fitting of the PC1

spectrum is shown as an example in Fig. 4(d). The function $T_{\mathrm{FPI}}(\lambda)$ reproduces the IR well shape better, whereas $T_0[1 - T_{\mathrm{FPI}}(\lambda)]$ loses accuracy in the peripherical regions but allows for simultaneous fitting of both bandgaps.

The spectrum of a nonlinear Fabry–Perot cavity shifts following the change in the refractive index complies with the following set:

$$n(I) = n_0 + n_2 I, \tag{5}$$

$$T_{\mathrm{FPI}}(\lambda, I) = \frac{T_{\mathrm{out}}}{1 + F\sin^2\left[\delta_0(\lambda) + \delta_{\mathrm{NL}}(\lambda) I\right]}, \tag{6}$$

$$\delta_{\mathrm{NL}}(\lambda) = \frac{2\pi}{\lambda} n_2 L. \tag{7}$$

At sufficiently low intensities, Eq. (6) can be represented by the first two terms of its Taylor expansion. Using the normalized transmittance at a certain wavelength, it can be rearranged to give

$$T_{\mathrm{norm}} \approx 1 - \frac{F\sin(2\delta_0)}{1 + F\sin^2(\delta_0)} \delta_{\mathrm{NL}} I. \tag{8}$$

On the other hand, the solution of Eq. (2) without saturation ($I_{\mathrm{sat},\alpha} = I_{\mathrm{sat},\beta} = \infty$) for normalized transmittance of the Gaussian beam gives

$$T_{\mathrm{norm}} = \sum_{m=0}^{\infty} (-1)^m (m+1)^{-3/2} (\beta_{\mathrm{eff}} L_{\mathrm{eff}} I)^m,$$
$$L_{\mathrm{eff}} = \left(1 - e^{-\alpha L}\right)/\alpha. \tag{9}$$

At low intensities, this sum can be truncated at $m = 1$. Consideration of $L_{\mathrm{eff}} = L$ is quite acceptable for our low absorption films. Then, comparing Eqs. (8) and (9) and considering Eq. (7), we obtain

$$n_2 \approx \frac{\lambda}{4\pi\sqrt{2}} f \beta_{\mathrm{eff}}. \tag{10}$$

Factors $f = F\sin(2\delta_0)/[1 + F\sin^2(\delta_0)]$ were calculated with F and δ_0 obtained from the fitting of the spectra by Eq. (4) and, together with the resulting n_2 values, they are as shown in Table 2.

According to [27], thermo-optic n_2 of graphene in solid films is positive (unlike that in liquid suspensions); its value is of the order of 10^{-5}–10^{-6} cm^2/W. At that, the studied film was crystalline, and graphene concentration ρ_{Gr} in it was close to that of the graphite, i.e., of the order 1 g/cm^3. Our estimations give $\rho_{\mathrm{Gr}} \sim 10^{-6}$ g/cm^3 in the 1DPCs. Considering this fact, we find our estimate of the n_2 value fairly plausible and evidently casting in favor of its thermo-optic nature because the Kerr n_2 must be eight orders of magnitude smaller and negative [27].

A previous study of the bulk Gr@PVK film with $\rho_{\mathrm{Gr}} \sim 10^{-3}$ g/cm^3 in the infrared range gives $n_2 = 0.032$ cm^2/GW [28], which is one order less than our result. This difference may be attributed to the enhancement of nonlinear coefficients entailing the NLO properties enhancement in the 1DPC according to its $F = 12$ [14]. The absence of noticeable NLO response to the ns radiation in PC3 is apparently the consequence of a low field enhancement factor ($f_{\mathrm{fe}} = 0.83$) at the probing wavelength.

C. Continuous and Quasi-Continuous Response

Resulting curves of the two-way (forward and backward) I-scan at 1064 nm for PC1, PC2, and PC3 are shown in Fig. 5. Differences between scans made by intensity increasing (black data) and decreasing (red data) can reveal optical bistability in the event it takes place in the sample.

An optical bistability loop is visible in PC1 at intensities >400–600 W/cm^2 [Figs. 5(a) and 5(c)], which is absent in PC2 [Fig. 5(b)]. The switching contrast is very low (within $\sim$5% of T) and barely exceeds experimental uncertainties. In PC3, the loop is much more pronounced [Fig. 5(e)] and apparently begins from intensities around 100 W/cm^2 [Fig. 5(d)]. Its character is different from that in PC1, whereas the latter bleaches with increasing intensity and PC3 darkens. At the same time, the reflection from PC3 increases, which confirms that the reason for the transmittance change is the bandgap shift. These observations suggest that we deal with a thermal-induced phase shift in our 1DPCs in which graphene is the heater, and an increase in graphene concentration (as it is in PC3) leads to a larger shift, the latter being a downshift because the testing wavelength (1064 nm) is shorter than the wavelength of the bandgap minimum of PC3 and larger than the bandgap minimum of PC1.

Another demonstration of the phase shift is obtained in the tunable qcw-Z-scan of PC1. We scanned the laser wavelength with a tunable femtosecond source over the IR bandgap and found SA, which increases when we move outside the bandgap toward the IR side [Fig. 6(a)]. We fitted the results using Eq. (9) with $m = 5$ and extracted nonlinear absorption β at each wavelength. This led us to the spectrum of β shown in Fig. 6(b).

Here again, the evident displacement of the bleaching coefficient with respect to the bandgap minimum gives evidence of a down phase-shift of PC1 under the qcw radiation: at larger intensities, it enhances the saturable absorption behavior. The down phase-shift is also different from what we have observed in the ns regime. Whereas we saw in the latter a manifestation of the thermo-optic nonlinearity of Gr@PVK and C_{60}@PVK composites, which is positive, here, we most probably deal with the thermal expansion of layers.

Polymers are characterized by significant values of the thermal expansion coefficient. The values for PVA and PVK are tabulated: $\alpha_t = 1.2 \cdot 10^{-4}$ K^{-1} and $\alpha_t = 5 \cdot 10^{-5}$ K^{-1}, respectively [18]. With these, the temperature coefficients of the optical path length, $ds/d\theta$, become negative [29], in particular, for PVA: $ds/d\theta = -1 \cdot 10^{-4}$ K^{-1}. This value determines the phase shift, and the corresponding shift of the bandgap minimum is

$$\Delta\lambda = 2\left(l_1 \frac{ds_1}{d\theta} + l_2 \frac{ds_2}{d\theta}\right)\Delta\theta. \tag{11}$$

Henceforth, Index 1 refers to the PVK layer, while Index 2 refers to the PVA layer. Thus, the heating value $\Delta\theta$ determines the shift unambiguously and requires an estimation.

The heat flux arising from the absorption of radiation by the PVK layers is obtained from the Lambert–Beer law:

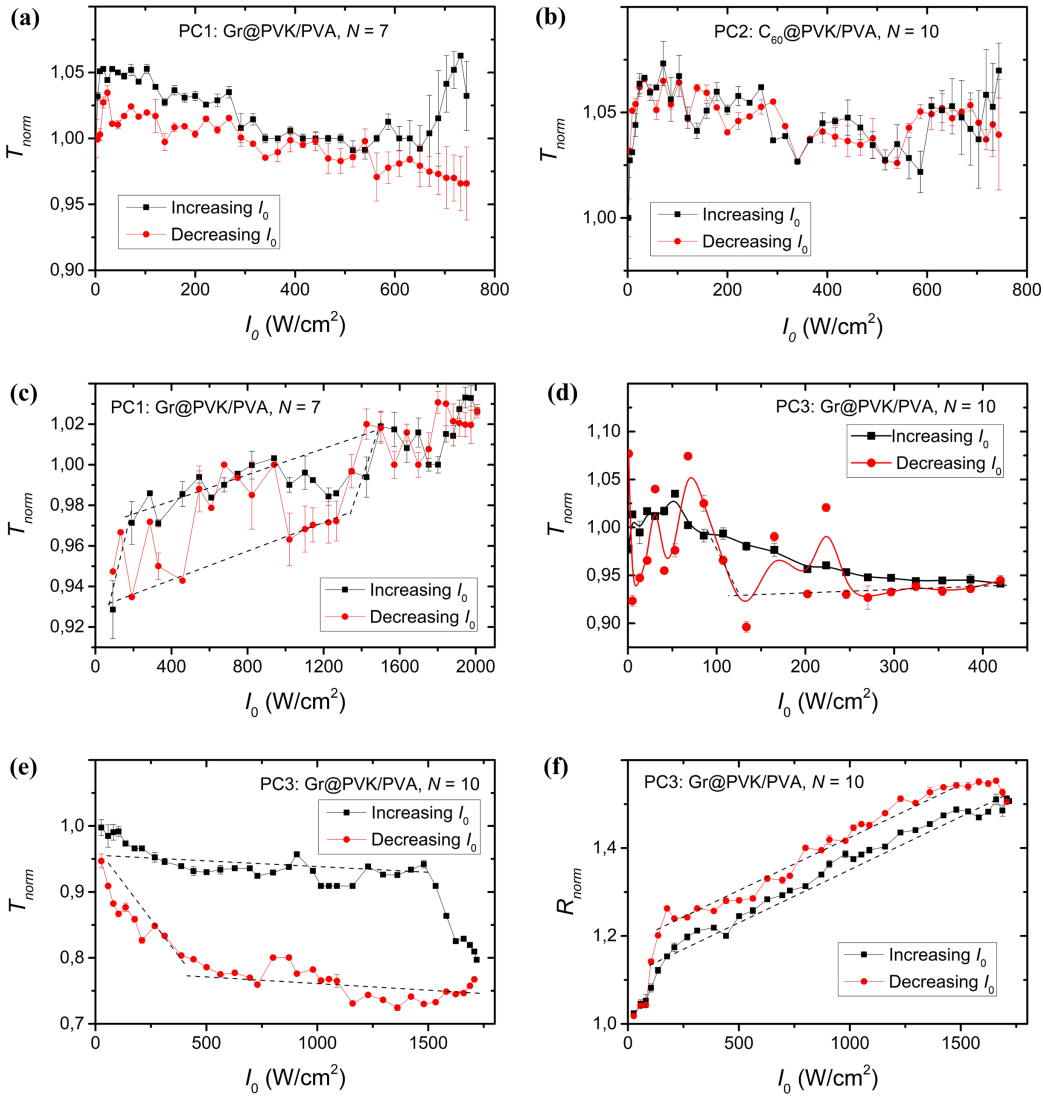

Fig. 5. Cw I-scan: normalized transmittance of (a), (c) PC1 in different intensity ranges, (b) PC2, (d), (e) PC3 in different intensity ranges, and (f) normalized reflectance of PC3.

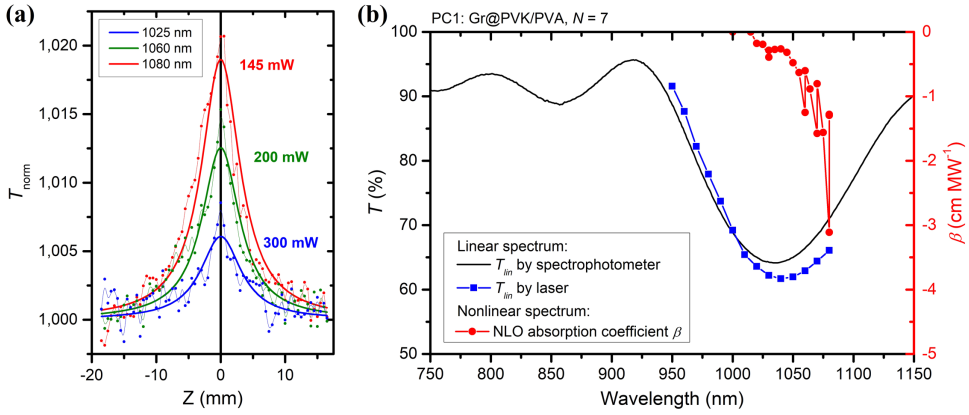

Fig. 6. (a) Z-scan curves of PC1 at different laser wavelengths. (b) Spectrum of its nonlinear absorption coefficient (red curve) in comparision with the linear transmittance (blue curve) extracted from the Z-scan experiment.

$$q_+ = I\left(1 - e^{-\sigma_{\mathrm{Gr}}\rho_{\mathrm{Gr}}^{p} N l_1}\right) \approx \sigma_{\mathrm{Gr}}\rho_{\mathrm{Gr}}^{p} N l_1 I, \qquad (12)$$

where I is the radiation intensity, σ_{Gr} is the average absorption cross-section of graphene particles in the suspension, ρ_{Gr}^{p} is the density of carbon dispersed in PVK, and N is the PC period number.

Heating of PCs was followed neither by light emission (it was controlled by IR camera) nor by visually noticeable fritting. This means that the temperature did not exceed polymer melting points, i.e., $\Delta\theta = \theta_{\mathrm{PC}} - \theta_{\mathrm{room}} < \sim 200$ K. Thus, major heat losses were due to the thermal conductivity. A quartz substrate with the width $l_3 = 1$ mm, which is three orders of magnitude larger than L, served in this configuration as a heat reservoir. We do not consider heat exchange with air because thermal resistance at the air–polymer interface is sufficiently higher. Thermal flux of losses caused by heat exchange between the multilayer wall of PCs and the ambient medium is

$$q_- = \frac{\Delta\theta}{\left(N\frac{l_1}{\lambda_1} + N\frac{l_2}{\lambda_2} + R_{P-Q} + \frac{l_3}{\lambda_3}\right)}, \qquad (13)$$

where λ_1, λ_2, and λ_3 are the thermal conductivity coefficients of PVK, PVA, and quartz, respectively; R_{P-Q} is the thermal resistance of the PVA-quartz interface. Here, we neglected the thermal resistance on the PVK/PVA interface, assuming that the thermal characteristics of the polymers are approximately the same, and the contact of the layers is sufficiently strong.

With a steady-state thermal process, the heat fluxes q_+ and q_- should be equal, which gives an estimate for the heating:

$$\Delta\theta = \sigma_{\mathrm{Gr}}\rho_{\mathrm{Gr}}^{p} N l_1 I\left(N\frac{l_1}{\lambda_1} + N\frac{l_2}{\lambda_2} + R_{P-Q} + \frac{l_3}{\lambda_3}\right). \qquad (14)$$

The value R_{P-Q} of the polymer-quartz contact depends not only on materials themselves but on many other factors such as morphology of the contacting surfaces. We were only able to find information about the contact of an amorphous polythiophene nanotube forest with a quartz substrate, suggesting R_{P-Q} in the diapason $0.1-1.5$ cm^2/WK [30]. We suppose that the thermal contact of PVA and quartz is not worse than the above-mentioned, taking into account the continuous character of the interface in our system. Using values $\sigma_{\mathrm{Gr}} = 5900$ cm^2/g [14], $\lambda_1 = \lambda_2 = 0.002$ W/cm K [18], and $\lambda_3 = 0.0135$ W/cm K [31] at intensity $I = 20$ kW/cm^2, which is reached at the peak in Z-scanning, the heating value of PC1 lies in the range of 31–36 K in accordance with the known range of R_{P-Q}. For comparison, in the case of PC3, the heating can be even 83–99 K.

At the same time, it should be noted that the heating value is directly proportional to the absorption cross-section of graphene, which can vary greatly, depending on the morphology of the particles, and reach larger values [16]. It can also vary depending on the particle density, the error in the estimation of which can be significant. Moreover, it can be increased if one takes into account interlayer thermal resistances that can occur in a real situation on the PVA/PVK interface. Meanwhile, the increase of thermal conductivity with the increase of temperature will result in better cooling. Thus, we suppose it is possible to estimate the heating in the vicinity of 100 K. At such heating, the minimum shift for PC1, calculated by Eq. (11), is 5 nm (we assume $ds_1/d\theta$ for PVK to be a half of $ds_2/d\theta$, taking into account the proportionally smaller thermal expansion coefficient of PVK).

An approximate relationship between the nonlinear absorption coefficient and the thermally induced shift of the 1DPC bandgap can be established using Eq. (10). For a Gaussian beam at focus ($z = 0$), one has

$$\beta_{\mathrm{te}} \approx \frac{2\sqrt{2}}{L_{\mathrm{eff}} T_{\mathrm{lin}}}\frac{dT}{dI} = \frac{2\sqrt{2}}{L_{\mathrm{eff}} T_{\mathrm{lin}}}\frac{dT}{d\lambda}\frac{d\lambda}{d\theta}\frac{d\theta}{dI}. \qquad (15)$$

The first derivative on the right-hand side of Eq. (15), together with the linear transmission T_{lin}, is found from the transmission spectra. In particular, for PC1 at a wavelength of 1064 nm, it holds $(T_{\mathrm{lin}})^{-1} dT/d\lambda = 3 \cdot 10^{-4}$ nm^{-1}. The other two derivatives are calculated from Eqs. (11) and (14), respectively: $d\lambda/d\theta = -0.05$ nm/K and $d\theta/dI = 2000$ cm^2 K/MW. Thus, we obtain the estimate for this thermal expansion NLO coefficient $\beta_{\mathrm{te}} \approx 680$ cm/MW.

Simultaneously with this shift, an opposite phase shift occurs, which results from the thermo-optical nonlinearity of graphene in PVK. The increment of the latter shift, according to estimates obtained in the nanosecond experiment, provides a commensurable value β_{to} (see Table 2). Due to a plethora of error sources, we cannot calculate the exact sum of these effects; however, the value that we see from the experiment [Fig. 6(b)], i.e., $\beta_{\mathrm{res}}(1064) \approx 1$ cm/MW is, presumably, the real measure of the combined action from these sources.

It is worth noting that an electrostrictive compression can also take place in the samples because the light field gradients inside the layers are significant, as is shown in Figs. 2(b), 2(d), and 2(f). This effect is considered in the supplemental materials (Supplement 1) and found too weak in PC1.

The inclusion of a photonic crystal in the feedback loop with the cw-laser resonator by adjusting the angle of its reflection allows us to obtain a mode in which spontaneous jumps of the transmitted signal occur, evidencing two clearly different states [Fig. 7(a)].

At the same time, in PC1, there is a switch from a higher transmission value to a lower one, which corresponds to a jump-like relaxation of thermal lenses in the FC layers and a reverse

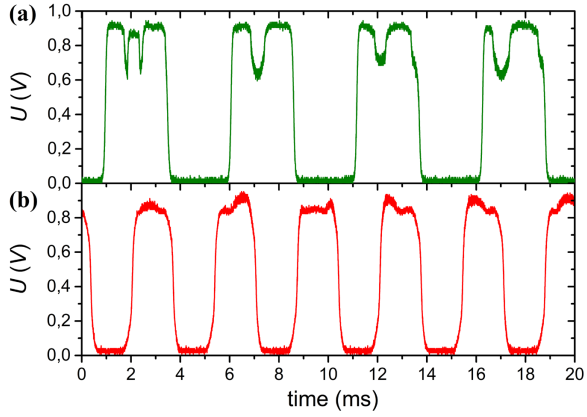

Fig. 7. Oscillograms of the amplitude-modulated signal transmitted through (a) PC1 and (b) PC3, coupled with the laser cavity.

shift of the bandgap. The switching has a threshold character and appears at intensities over ~2 kW/cm^2. A similar coupling of a pure quartz substrate and PC2 with the resonator reveals only chaotic fluctuations in the signal level, with an order of magnitude smaller amplitude. When it comes to PC3, we also observed a chaotic switching, smaller in amplitude than in the case of PC1, in the direction of a greater transmission [Fig. 7(b)], which corresponds to a different sign of the derivative of this 1DPC. Thus, the indistinct bistability of 1DPC can be shown when used in a resonator mode, which prompts the paths of further improvement in the design of optical switches.

D. Femtosecond Response and Ultrafast Dynamics

Femtosecond I-scan curves obtained at 520 and 1040 nm for all 1DPCs as well as for bulk Gr@PVK and C_{60}@PVK films are shown in Fig. 8. More attention was paid to the visible region where the bandgaps are narrower and C_{60} has absorption bands.

An obvious SA behavior is seen for PC1, PC2, and the corresponding bulk films. As noticed for the ns case, the fs response of PC3 is also linear because its bandgap is far from the laser wavelength, and the weakening of the field takes place within its structure at the bandgap wing. The nonlinear transmission function shows a threshold character, which is not typical for standard SA models. This indicates a multiplicity of processes occurring. We could fit the results only by putting a threshold intensity I_{th}, under which T is strictly linear. Above the threshold, the function is well fitted by the model of SA with saturable TPA in homogeneously broadened systems, as described by Eq. (2) with $n_\alpha = n_\beta = 2$. The fitting curves are shown as solid lines in Fig. 8(a), and their parameters are given in Table 3.

It is important to note that the scanning intensities were larger than those in our previous study [14], where the SA effect was seen at several MW/cm^2. Here, we see another effect, and its unusual saturation character strongly interfering with a positive NLO absorption may indicate the influence of optical switching due to a fast phase shift. For comparison, the I-scan curves obtained with bulk C_{60}@PVK and Gr@PVK films are remarkably smoother. From Table 3, we see that the saturation intensity stays the same in all of the samples and apparently is related neither to 1DPC structure, nor to nanoparticles, but likely to a process in the polymer matrix. At the same time, we see a significant increase in β in PCs with respect to bulk films. Its saturation is apparently caused by the short pulse compared with the electron relaxation time, which is stronger than the bandgap shifting effect and is equally manifested both in PCs and in bulk films. However, we can attribute the observed difference in β to the bandgap shift and the n_2 value, which is responsible, as evident in Eq. (10). The resulting values are given in Table 3.

In order to directly observe this fast shift, we performed a time-resolved spectral pump-probe of the PC structures in the visible region using the same laser source. No temporal changes were found in the Gr-containing PCs. At the same time, some changes are seen in PC2, especially those relating to the excitation of the C_{60} singlet-singlet absorption bands at $\lambda < 500$ nm. Three of the transient spectra obtained for PC2 at different time delays are shown in Fig. 9(a) in terms of transient absorption change: $\Delta A = 1 - T_{\text{pump on}}/T_{\text{pump off}}$.

In the C_{60}-containing PC, we found a hole in its transient spectrum near the bandgap. The same effect was guessed at twice lower intensity, but it was on the verge of detection. It can be described by its spectral shift: We reproduced the pit [black curve in Fig. 9(a)] by using the linear spectrum of PC2 as T_{initial} or $T_{\text{pump off}}$, and the same spectrum shifted by $\Delta\lambda = 8$ nm as $T_{\text{pump on}}$. This pit disappears in time. The area S shown in Fig. 9(a) by a triangle approximates the integral intensity of this

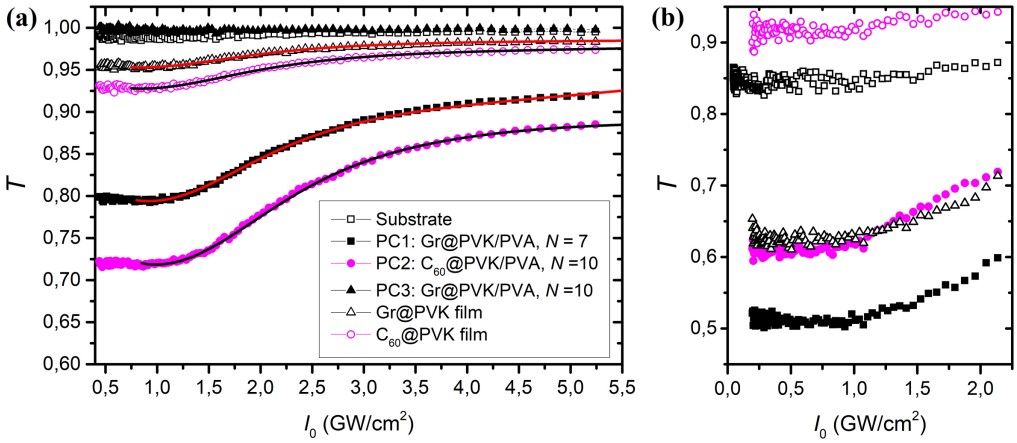

Fig. 8. Transmittance in fs I-scan of 1DPCs at (a) 520 nm and (b) 1040 nm. The legend is valid for both plots.

Table 3. NLO Characteristics of 1DPCs Obtained from fs I-Scan at 520 nm

Sample	I_{th} (GW/cm^2)	$I_{sat,\alpha}$ (GW/cm^2)	β (cm/GW)	$I_{sat,\beta}$ (GW/cm^2)	n_2 (10^{-4} cm^2/GW)
PC1	0.80	1.40	195	6	1.4
PC2	0.82	1.44	210	4.8	3.6
Gr@PVK	0.75	1.40	40	6	–
C_{60}@PVK	0.75	1.40	70	5	–

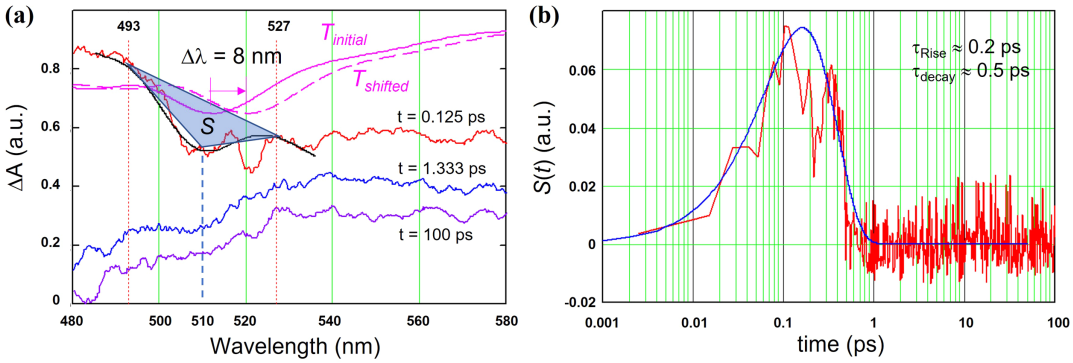

Fig. 9. (a) Transient spectra of PC2 obtained at $I_{pump} = 23$ GW/cm^2. (b) Time profile of the marked triangle area.

bandgap "burning." Its evolution in time is shown in Fig. 9(b) and is well fitted by a single exponent with the autocorrelation of the pump and probe pulses [32]:

$$S(t) = Ae^{-t/\tau_d}(1 - e^{-t/\tau_R})\left[1 + \mathrm{erf}\left(\frac{\tau_p}{\sqrt{2}\tau_d} - \frac{t}{\sqrt{2}\tau_p}\right)\right], \quad (16)$$

where τ_R is the rise time and τ_d is the decay time, which turns out to be ultrashort: $\tau_R \approx 0.2$ ps and $\tau_d \approx 0.5$ ps. The spectral shift corresponds to the nonlinear refractive index:

$$n_2 \approx \frac{\Delta\lambda}{2Nl_1 I}. \quad (17)$$

The value $n_2 \approx 1 \cdot 10^{-4}$ cm^2/GW turns out to be of the same order as the one found from the I-scan (Table 3). For a C_{60}@silane composite, the nonresonant third-order optical susceptibility $\chi^{(3)} = 1.6 \cdot 10^{-13}$ esu was measured at 860 nm [33]. This value corresponds to the Kerr $n_2 \approx 2 \cdot 10^{-6}$ cm^2/GW. Our result is two orders of magnitude larger, partially because of a resonance with C_{60} absorption bands but mainly due to the photonic crystal enhancement. The latter conclusion comes from the fact that we see the same order of n_2 in PC1; however, the sensitivity of the transient spectra registration is not sufficient to resolve its bandgap shift. Therefore, we obtained 1DPCs with the Kerr nonlinear refraction coefficients, which can provide ultrafast, sub-picosecond switching over the threshold of around 0.8 GW/cm^2. The improvement of its performance can be achieved by further increasing graphene concentration in PVK layers and Q-factors of the bandgaps (by increasing the number of periods and refining the layers homogeneity).

A summary of the NLO effects taking place at different time scales in the 1DPCs under study is given in Table 4. Thermo-optic relaxation time was not evaluated in our study. For dispersed nanoparticles, it is known to be strongly dependent on nanoparticle morphology and surrounding: from 1 ns for a single-layer graphene [34] to several hundred μs for multilayer and wrinkled graphene [35].

4. CONCLUSION

We produced 1D photonic crystals (1DPCs) of alternating layers of poly(vinyl carbazole) (PVK)/poly(vinyl alcohol) (PVA) with seven and 10 periods containing inclusions of fullerene and graphene in PVK using the ordinary spin-coating procedure. The crystals have two bandgaps, i.e., at different wavelengths in the IR and in the visible regions and are characterized by Q-factors around 10 and contrast around 5. The light field enhancement inside the multilayer structures at their bandgap has been calculated by matrix calculations. The nonlinear optical transmission of the samples at $\lambda = 1064$ nm has been studied by I- and Z-scans with ns, cw, and qcw femtosecond laser radiation. The samples demonstrate the predominance of an optical limiting behavior in ns regime around the IR bandgap, the effect being stronger in a graphene-containing sample (PC1). It was explained by the thermo-optic (fast) nonlinearity of Gr@PVK and C_{60}@PVK composites, the found values being of the order $n_2^{to} \sim 10^{-1}$ cm^2/GW.

In the cw regime, either bleaching or limiting is seen, depending on which side of the laser wavelength the bandgap is located. A bistability loop has been found in the nonlinear transmittance and nonlinear reflectance functions of graphene-containing samples, being more pronounced in the sample with a higher graphene concentration. The characteristic intensity threshold amounts the order of 100 W/cm^2. A manifestation of the same character phase-shifting has been found in a spectrum of the nonlinear absorption coefficient of PC1 obtained in the qcw regime. The observed behavior is explained in terms of the combined action of opposing thermal expansion (slow) nonlinearity and the thermo-optic one with characteristic NLO coefficients of the same order. The slow bistablity relating to the thermal

Table 4. NLO Effects Observed in the 1DPCs and Their Typical Characteristics

Time Range	Typical Relaxation Time	Typical n_2 (cm^2/GW)	NLO Effect in Action
Millisecond—Continuous	10 μs	-10^{-1} to -1	Thermal expansion
Nanosecond	1 ns–100 μs	$+10^{-1}$	Thermo-optic refraction
Femtosecond	0.5 ps	$+10^{-4}$	Optical Kerr effect

expansion has been demonstrated in the spontaneous switching of the cw laser output.

An ultrafast switching was found in both graphene- and fullerene-containing 1DPCs (PC1 and PC2, respectively) within their visible bandgaps. A remarkable redshift of the bandgap of PC2 was demonstrated in its transient absorption spectra. The shift relates to the positive nonlinearity of the same order, which causes the switching: $n_2^{\mathrm{Kerr}} \sim 10^{-4}$ cm^2/GW. Subpicosecond rise and decay times of this shift were obtained. They pointed at an ultrafast Kerr process, which can be used for the elaboration of ultrafast optical bistability by further adjusting nanoparticle concentration and film quality.

We therefore show that polymer 1DPCs processed from Gr@PVA and C_{60}@PVA composite possess nonlinear optical properties in the spectral regions around their bandgap, with both slow and fast bistable behavior, whose parameters can be improved with increasing the number of layers and concentration of nanoparticles. Such compact structures are easy and affordable in manufacturing and may be a good platform for on-chip all-optical switches.

Funding. Strategic Priority Research Program of CAS (XDB16030700, XDB43010303); Natural Sciences and Engineering Research Council of Canada (RGPIN-2020-07016); CAS President's International Fellowship Initiative (2021VTB0003); Shanghai Science and Technology International Cooperation Fund (19520710200, 19520743900).

Disclosures. The authors declare no conflicts of interest.

Data Availability. Data underlying the results presented in this paper are not publicly available at this time but may be obtained from the authors upon reasonable request.

Supplemental document. See Supplement 1 for supporting content.

REFERENCES

1. H. M. Gibbs, S. L. McCall, and T. N. C. Venkatesan, "Differential gain and bistability using a sodium-filled Fabry-Perot interferometer," Phys. Rev. Lett. **36**, 1135–1138 (1976).
2. T. Alexoudi, G. T. Kanellos, and N. Pleros, "Optical RAM and integrated optical memories: a survey," Light Sci. Appl. **9**, 91 (2020).
3. D. Smirnova, D. Leykam, Y. Chong, and Y. Kivshar, "Nonlinear topological photonics," Appl. Phys. Rev. **7**, 021306 (2020).
4. B. J. Shastri, A. N. Tait, T. Ferreira de Lima, W. H. P. Pernice, H. Bhaskaran, C. D. Wright, and P. R. Prucnal, "Photonics for artificial intelligence and neuromorphic computing," Nat. Photonics **15**, 102–114 (2021).
5. H. M. Gibbs, S. L. McCall, T. N. C. Venkatesan, A. C. Gossard, A. Passner, and W. Wiegmann, "Optical bistability in semiconductors," Appl. Phys. Lett. **35**, 451–453 (1979).
6. H. M. Gibbs, S. S. Tarng, J. L. Jewell, D. A. Weinberger, K. Tai, A. C. Gossard, S. L. McCall, A. Passner, and W. Wiegmann, "Room-temperature excitonic optical bistability in a GaAs-GaAlAs superlattice etalon," Appl. Phys. Lett. **41**, 221–222 (1982).
7. A. A. Ryzhov, Y. Wang, H. Qi, and J. Wang, "Optical limiting properties of a nonlinear multilayer Fabry-Perot resonator containing niobium pentoxide as nonlinear medium," Opt. Lett. **39**, 4847–4850 (2014).
8. J. N. Acharyya, D. N. Rao, M. Adnan, C. Raghavendar, R. B. Gangineni, and G. V. Prakash, "Giant optical nonlinearities of photonic minibands in metal-dielectric multilayers," Adv. Mater. Interfaces **7**, 2000035 (2020).
9. A. R. Cowan and J. F. Young, "Nonlinear optics in high refractive index contrast periodic structures," Semicond. Sci. Technol. **20**, R41–R56 (2005).
10. J. Shiri, J. Khalilzadeh, and S. H. Asadpour, "Optical bistability in reflection of the laser pulse in a 1D photonic crystal doped with four-level InGaN/GaN quantum dots," Laser Phys. **31**, 036202 (2021).
11. M. F. Weber, C. A. Stover, L. R. Gilbert, T. J. Nevitt, and A. J. Ouderkirk, "Giant birefringent optics in multilayer polymer mirrors," Science **287**, 2451–2456 (2000).
12. T. Fryett, A. Zhan, and A. Majumdar, "Cavity nonlinear optics with layered materials," Nanophotonics **7**, 355–370 (2018).
13. Q. Quan, I. B. Burgess, S. K. Y. Tang, D. L. Floyd, and M. Loncar, "High-Q, low index-contrast polymeric photonic crystal nanobeam cavities," Opt. Express **19**, 22191–22197 (2011).
14. S. Zhang, C. Shen, I. M. Kislyakov, N. Dong, A. Ryzhov, X. Zhang, I. M. Belousova, J.-M. Nunzi, and J. Wang, "Photonic-crystal-based broadband graphene saturable absorber," Opt. Lett. **44**, 4785–4788 (2019).
15. N. N. Lepeshkin, A. Schweinsberg, G. Piredda, R. S. Bennink, and R. W. Boyd, "Enhanced nonlinear optical response of one-dimensional metal-dielectric photonic crystals," Phys. Rev. Lett. **93**, 123902 (2004).
16. M. Lotya, P. J. King, U. Khan, S. De, and J. N. Coleman, "High-concentration, surfactant-stabilized graphene dispersions," ACS Nano **4**, 3155–3162 (2010).
17. I. M. Kislyakov, J.-M. Nunzi, X. Zhang, Y. Xie, V. N. Bocharov, and J. Wang, "Stimulated Brillouin scattering in dispersed graphene," Opt. Express **26**, 34346 (2018).
18. G. Wypych, *Handbook of Polymers*, 2nd ed. (ChemTech, 2016).
19. D. S. Bethune, "Optical harmonic generation and mixing in multilayer media: analysis using optical transfer matrix techniques," J. Opt. Soc. Am. B **6**, 910 (1989).
20. M. J. Schnepf, M. Mayer, C. Kuttner, M. Tebbe, D. Wolf, M. Dulle, T. Altantzis, P. Formanek, S. Förster, S. Bals, T. A. F. König, and A. Fery, "Nanorattles with tailored electric field enhancement," Nanoscale **9**, 9376–9385 (2017).
21. V. Bermudez, F. Kajzar, S. Niziol, J. Niziol, J. Pielichowski, J. Sanetra, and D. Bogdal, "Linear and nonlinear optical properties of polyvinyl carbazaol and polyvinyl carbazol substitued thin films," Proc. SPIE **4106**, 165–176 (2000).
22. S. L. Ren, Y. Wang, A. M. Rao, E. McRae, J. M. Holden, T. Hager, K. A. Wang, W.-T. Lee, H. F. Ni, J. Selegue, and P. C. Eklund, "Ellipsometric determination of the optical constants of C_{60} (Buckminsterfullerene) films," Appl. Phys. Lett. **59**, 2678–2680 (1991).
23. D. E. Aspnes, "Optical properties of thin films," Thin Solid Films **89**, 249–262 (1982).
24. A. Benchaabane, Z. B. Hamed, F. al Kouki, M. A. Sanhoury, K. Zellama, A. Zeinert, and H. Bouchriha, "Performances of effective medium model in interpreting optical properties of polyvinyl-carbazole: ZnSe nanocomposites," J. Appl. Phys. **115**, 134313 (2014).
25. N. Dong, Y. Li, S. Zhang, N. McEvoy, R. Gatensby, G. S. Duesberg, and J. Wang, "Saturation of two-photon absorption in layered transition metal dichalcogenides: experiment and theory," ACS Photon. **5**, 1558–1565 (2018).
26. E. Hecht, *Optics* (Addison Wesley, 2002), Chap. 9.
27. R. Weigand, M. Sánchez-Balmaseda, S. M. Afanador-Delgado, and H. J. Salavagione, "Nonlinear thermal and electronic optical properties of graphene in N-methylpyrrolidone at 800 nm with femtosecond laser pulses," J. Appl. Phys. **124**, 033104 (2018).
28. A. D. Grishina, T. V. Krivenko, V. V. Savel'ev, R. W. Rychwalski, and A. V. Vannikov, "Photoelectric, nonlinear optical, and photorefractive properties of polyvinylcarbazole composites with graphene," High Energy Chem. **47**, 46–52 (2013).
29. V. Pilla, T. Catunda, D. T. Balogh, R. M. Faria, and S. C. Zilio, "Thermal lensing in poly(vinyl alcohol)/polyaniline blends," J. Polym. Sci. B **40**, 1949–1956 (2002).
30. V. Singh, T. L. Bougher, A. Weathers, Y. Cai, K. Bi, M. T. Pettes, S. A. McMenamin, W. Lv, D. P. Resler, T. R. Gattuso, D. H. Altman, K. H. Sandhage, L. Shi, A. Henry, and B. A. Cola, "High thermal conductivity of chain-oriented amorphous polythiophene," Nat. Nanotechnol. **9**, 385–390 (2014).
31. V. I. Sviridenko, V. A. Medvedev, N. P. Rybkin, and V. G. Gorbunova, "The thermal conductivity of KV fused silica at 2–300°K," Meas. Tech. **30**, 454–458 (1987).

32. D. J. Hilton, "Ultrafast pump-probe spectroscopy," in *Optical Techniques for Solid-State Materials Characterization*, R. P. Prasankumar and A. J. Taylor, eds. (CRC Press, 2012).
33. B. L. Yu, H. P. Xia, C. S. Zhu, and F. X. Gan, "Enhanced third-order nonlinear optical properties of C_{60}-silane compounds," Appl. Phys. Lett. **81**, 2701–2703 (2002).
34. W. Chen, G. Wang, S. Qin, C. Wang, J. Fang, J. Qi, X. Zhang, L. Wang, H. Jia, and S. Chang, "The nonlinear optical properties of coupling and decoupling graphene layers," AIP Adv. **3**, 042123 (2013).
35. S. Dey, S. R. Bongu, V. K. Sagar, and P. B. Bisht, "Investigation of thermal nonlinearity due to nJ high repetition rate fs pulses on wrinkled graphene," J. Opt. Soc. Am. B **38**, 2019–2026 (2021).